RocS drives chromosome segregation and nucleoid protection in *Streptococcus pneumoniae*

Chryslène Mercy[1], Adrien Ducret [1], Jelle Slager[2], Jean-Pierre Lavergne[1], Céline Freton[1], Sathya Narayanan Nagarajan [1], Pierre Simon Garcia[1], Marie-Francoise Noirot-Gros[3,5], Nelly Dubarry[1,6], Julien Nourikyan [1], Jan-Willem Veening [2,4] and Christophe Grangeasse [1]*

Chromosome segregation in bacteria is poorly understood outside some prominent model strains[1-5] and even less is known about how it is coordinated with other cellular processes. This is the case for the opportunistic human pathogen *Streptococcus pneumoniae* (the pneumococcus)[6], which lacks the Min and the nucleoid occlusion systems[7], and possesses only an incomplete chromosome partitioning Par(A)BS system, in which ParA is absent[8]. The bacterial tyrosine kinase[9] CpsD, which is required for capsule production, was previously found to interfere with chromosome segregation[10]. Here, we identify a protein of unknown function that interacts with CpsD and drives chromosome segregation. RocS (Regulator of Chromosome Segregation) is a membrane-bound protein that interacts with both DNA and the chromosome partitioning protein ParB to properly segregate the origin of replication region to new daughter cells. In addition, we show that RocS interacts with the cell division protein FtsZ and hinders cell division. Altogether, this work reveals that RocS is the cornerstone of a nucleoid protection system ensuring proper chromosome segregation and cell division in coordination with the biogenesis of the protective capsular layer.

Previous studies have shown that pneumococcal chromosome partitioning-protein ParB and *Streptococcus pneumoniae* condensin (SMC) are involved, but not essential, in pneumococcal chromosome segregation[8]. Notably, individual or double deletion of *parB* and *smc* only lead to weak chromosome segregation defects, suggesting that other factors remain to be discovered. In line with this hypothesis, impaired autophosphorylation of the bacterial tyrosine kinase (BY-kinase) CpsD generated elongated cells with an aberrant nucleoid morphology[10]. CpsD is primarily described as a key regulator of the export and synthesis of the polysaccharide capsule, the main virulence factor of the pneumococcus, which is exclusively produced at the pneumococcal division septum[10-13]. To understand the potential relationship between capsule production and the chromosome biology, we first screened a yeast two-hybrid genomic library of a pneumococcal laboratory strain[14] using CpsD or its membrane activator CpsC as baits. Indeed, the interaction between CpsD and CpsC mimics the behaviour of BY-kinases found in proteobacteria[15]. Both CpsD and CpsC interacted with Spr0895, a protein with unknown function (Supplementary Fig. 1a). The interaction between Spr0895 and CpsD was confirmed in vitro and in vivo (Supplementary Fig. 1b–d). The *spr0895* gene is

conserved among Streptococcaceae (Supplementary Fig. 2) and is hereinafter referred to as *rocS* (encoding Regulator of Chromosome Segregation) based on our observations below.

We first deleted *rocS* in the encapsulated virulent D39 strain and analysed capsule production by immunofluorescence microscopy[10]. As observed for wild-type (WT) cells, capsule was detected over the entire surface of Δ*rocS* cells (Fig. 1a). Quantification of the fluorescent signal, together with the immuno-detection of the total fraction of capsule, revealed that capsule production and polymerization were not affected (Supplementary Fig. 3). However, although the cell shape of Δ*rocS* cells was not significantly altered, mutants displayed a growth defect with an increased generation time compared with WT cells (Supplementary Fig. 4). Surprisingly, when we looked at the DNA content of Δ*rocS* cells, we found that 13.9% of cells were anucleate (Fig. 1a,b). Deletion of *rocS* in the isogenic non-encapsulated mutant D39Δ*cps* or the non-encapsulated laboratory R800 strain resulted in comparable fractions (15.4% and 15.7%, respectively) of anucleate cells (Fig. 1b and Supplementary Figs. 5 and 6), indicating that nucleoid defects were not dependent on capsule production. Complementation of the Δ*rocS* D39 and R800 mutants with an ectopic copy of *rocS* (Δ*rocS*-P$_{comX}$-*rocS*) restored the WT phenotype with 1.5% and 1% of anucleate cells, respectively (Fig. 1b). By comparison, the deletion of *parB* or *smc* results in less than 4% of anucleate cells[8]. Thus, we deleted *parB* or *smc* in the D39-Δ*rocS*-P$_{comX}$-*rocS* strain. On *rocS* induction, these mutants were as viable as the Δ*rocS* D39 mutant. However, the depletion of *rocS* induced an additive detrimental effect on cell viability (Supplementary Fig. 7). Consistently, we were unable to delete both *rocS* and either *smc* or *parB*, suggesting that RocS acts complementary with ParB and SMC in the pneumococcal chromosome biology.

To analyse the chromosome dynamics in the absence of RocS, we quantified the relative proportions of three size groups (small, elongated and constricting cells) for Δ*rocS* R800 cells (Fig. 1c). By comparison with the relative proportion observed for WT cells, we observed an increase in the number of small cells: 62.5% of Δ*rocS* cells displayed the morphology of rounded small cells, whereas only 35% of WT cells harboured this morphology (Fig. 1c). As the formation of mini cells is usually associated with an aberrant localization of the divisome, we looked at its localization in Δ*rocS* cells using green fluorescent protein (GFP)-FtsA as a proxy. As observed for WT cells, GFP-FtsA localized at the division site at mid-cell in Δ*rocS* cells, suggesting that the localization of the division

[1]Molecular Microbiology and Structural Biochemistry, UMR 5086, Université Claude Bernard Lyon 1, Centre National de la Recherche Scientifique, Lyon, France. [2]Molecular Genetics Group, Groningen Biomolecular Sciences and Biotechnology Institute, Centre for Synthetic Biology, University of Groningen, Groningen, The Netherlands. [3]Micalis Institute, UMR1319, INRA, AgroParisTech, Université Paris-Saclay, Jouy-en-Josas, France. [4]Department of Fundamental Microbiology, Faculty of Biology and Medicine, University of Lausanne, Biophore Building, Lausanne, Switzerland. [5]Present address: Biosciences Division, Argonne National Laboratory, Lemont, IL, USA. [6]Present address: Evotec ID, Marcy l'Etoile, France. *e-mail: c.grangeasse@ibcp.fr
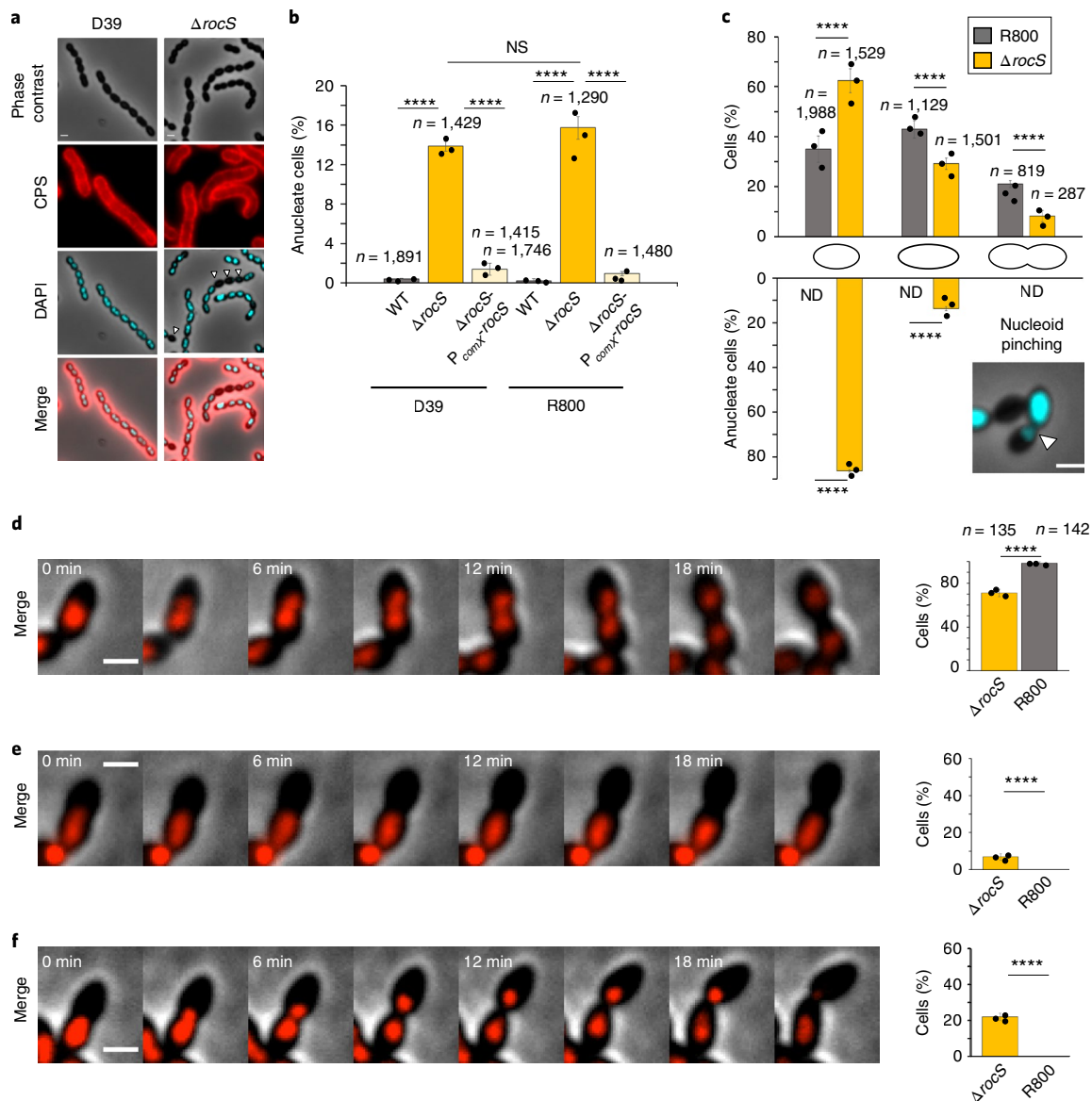
Fig. 1 | Effect of *rocS* deletion on capsule production and nucleoid distribution. a, Detection of CPS and DNA (stained with DAPI) in D39 and Δ*rocS* cells. The arrowheads indicate anucleate cells. Images are representative of three experiments repeated independently. **b**, Percentage of anucleate cells in D39 and R800 (grey) strains, corresponding Δ*rocS* mutants (yellow) and complemented strains (light yellow). **c**, Percentage of anucleate cells in the course of the cell cycle. R800 and Δ*rocS* cells were sorted into three size groups (from left to right: small, elongated and constricting cells) as a proxy for their progression in the cell cycle. The percentage of each group and the percentage of anucleate cells in each group are shown in the upper and the lower bar charts, respectively. The arrowhead indicates chromosome pinching in constricting cells. ND, not detected. **d–f**, Still images from fluorescence time-lapse microscopy (Supplementary Videos 1–3) showing a normal nucleoid segregation (**d**), an absence of nucleoid segregation (**e**) or a nucleoid pinching event (**f**) during cell division in WT cells (**d**) or in Δ*rocS* cells (**e,f**) producing HlpA-mKate2. The percentage of each event (normal, absence or pinching) in WT and Δ*rocS* cells are shown in the corresponding bar charts. Scale bars, 1 μm. In **b–f**, *n* indicates the number of cells analysed from three independent experiments. The bars, with data points overlapping, represent the mean ± s.e.m. Two-tailed *P* values were derived from two-population proportion tests for the following pairs of proportions: **b**: D39-WT versus D39-Δ*rocS* ($P < 0.0001$); D39-Δ*rocS* versus D39-Δ*rocS*-P_{comX}-*rocS* ($P = 2.49 \times 10^{-12}$); R800-WT versus R800-Δ*rocS* ($P < 0.0001$); R800-Δ*rocS* versus R800-Δ*rocS*-P_{comX}-*rocS* ($P < 0.0001$); D39-Δ*rocS* versus R800-Δ*rocS* ($P = 0.158$). Upper panel **c**: R800-WT versus R800-Δ*rocS* small cells ($P < 0.0001$), elongated cells ($P < 0.0001$) and constricting cells ($P = 7.29 \times 10^{-12}$). Lower panel **c**: R800-WT versus R800-Δ*rocS* for small cells ($P < 0.0001$) and elongated cells ($P < 0.0001$). Panels **d–f**: R800-WT versus R800-Δ*rocS* $P = 2.6 \times 10^{-15}$ (**d**), $P = 8.2 \times 10^{-15}$ (**e**) and $P = 3.45 \times 10^{-5}$ (**f**). ****$P < 0.0001$. NS, not significant ($P > 0.05$).

machinery was not affected in Δ*rocS* cells (Supplementary Fig. 8). Remarkably, the small cells constitute the large majority of the anucleate cells (86.3%), whereas elongated and constricting cells harboured asymmetric distribution of the nucleoid, suggesting that chromosome pinching events occurred in Δ*rocS* cells (Fig. 1c). To confirm this, we followed the localization of the HlpA-mKate2

fusion, a pneumococcal histone-like protein[16]. As expected for WT cells, the chromosome duplicates at the early stage of the cell cycle and eventually splits into two parts that segregate to each daughter cell (Fig. 1d and Supplementary Video 1). By contrast, newly replicated chromosomes in Δ*rocS* cells were either not segregated (7%) (Fig. 1e and Supplementary Video 2) or partially segregated and

eventually truncated by the newly forming septum (21.8%), a process also known as the guillotine effect[17] (Fig. 1f and Supplementary Video 3). In the latter case, the signal of the truncated chromosome was ultimately degraded. In both cases, these aberrant chromosome partitioning events led to the formation of small and anucleate cells. To test whether chromosome replication was affected in the ΔrocS R800 mutant cells, we determined the ratio between the origin of replication (oriC) and the terminus region (ter) of the chromosome in exponentially growing cells[18] (Supplementary Fig. 9). As expected, we observed that WT cells displayed a characteristic mean ratio of 1.68 ± 0.28, whereas this ratio was close to 1 for a thermosensitive dnaA (encoding the replication initiator protein) mutant shifted to non-permissive temperature. The origin-to-terminus ratios of ΔrocS (1.67 ± 0.24) and complemented ΔrocS-P_{comX}-rocS (1.56 ± 0.24) cells were similar to that of WT cells, indicating that RocS is not involved in chromosome replication. Together, our results show that chromosome segregation rather than chromosome replication is severely affected in the absence of RocS.

To characterize the contribution of RocS to chromosome segregation, we next examined the localization of oriC during the cell cycle of WT and ΔrocS R800 cells (Fig. 2). We used a system based on the ectopic production of a fluorescent fusion of RepC, the ParB homologue of *Enterococcus faecalis*, and insertion of $parS_{Ef}$ sites from *E. faecalis* near the pneumococcal oriC[19] (Fig. 2a). Neither the expression of repC-gfp nor the insertion of $parS_{Ef}$ sites influenced the pneumococcal cell cycle as evidenced by WT growth kinetics and cell morphology (Supplementary Fig. 10). When produced, the RepC-GFP fusion formed diffraction-limited foci in the vicinity of oriC (Fig. 2b and Supplementary Fig. 10). As previously characterized[20], oriC localized as a single focus located around mid-cell of nascent cells (Fig. 2b). The duplication of the focus was followed by rapid segregation of the two foci towards the centre of each daughter cell where they remain as the cell elongates. Interestingly, new cycles of chromosome replication and segregation started early in the cell cycle, even before the completion of division, as attested by the 4.5% of nascent cells containing 2 foci and the 5% of cells at the later stage of the cell cycle containing 3 or 4 foci (Fig. 2b,c). By comparison, the subcellular localization of oriC throughout the cell cycle was strongly affected in the absence of RocS. After duplication, most of the two foci remained near mid-cell and did not segregate (Fig. 2b,c). On average, the spacing rate (the distance between 2 foci of oriC in relation to the cell length) was significantly lower in ΔrocS cells (0.32 ± 0.003) than in WT cells (0.47 ± 0.003) (Fig. 2d). Furthermore, the proportion of cells with single foci was significantly higher in ΔrocS cells (47.6%) than in WT cells (23%) (Fig. 2c). As chromosome replication was not affected in ΔrocS cells (Supplementary Fig. 9), this observation suggests that, after replication, some oriC copies may be too close to be detected as separated foci in ΔrocS cells. Finally, we did not detect constricting cells containing three or four foci in ΔrocS cells (Fig. 2c). Thus, the two newly replicated chromosome origins segregate less efficiently in the absence of RocS, reflecting its crucial role in chromosome segregation.

Next, we followed the subcellular localization of RocS fused to GFP (GFP-RocS). Expression and functionality of the GFP-RocS fusion is suitable for RocS localization studies as attested by WT growth kinetics, cell morphology, intracellular RocS level and a low level of anucleate R800 cells (3%) (Supplementary Figs. 11 and 12). By wide-field epifluorescence microscopy, the GFP-RocS fusion protein was shown to form one or two bright foci per cell that were mostly localized around mid-cell of small cells and that positioned towards the centre of the daughter cell as cells elongate (Fig. 3a). However, when observed by total internal reflection fluorescence microscopy at relatively high-frequency data acquisition, we also detected some highly dynamic but very faint foci with no specific localization during the cell cycle (Supplementary Fig. 13

and Supplementary Video 4). Using image averaging, we showed that the faint foci were homogeneously distributed all around the cell periphery. This suggested that the faint foci could represent small units of RocS diffusing to the cell membrane even if one cannot exclude that they could also be due to some degradation species of GFP-RocS (Supplementary Fig. 12). Interestingly, we observed that bright foci mostly colocalized with oriC (distance of $<0.15\,\mu m$; Supplementary Fig. 14), suggesting that only the bright foci might be involved in chromosome segregation. Supporting this, we detected that RocS interacts with the pneumococcal ParB protein both in vivo and in vitro (Supplementary Fig. 15). As ParB binds to four parS sites close to oriC[8], these data suggest that RocS acts together with ParB to allow proper chromosome segregation.

Bioinformatic analysis of the RocS sequence predicted the presence of a carboxy-terminal membrane-binding amphipathic helix (AH) homologous to that of MinD of *Escherichia coli*[21] and an amino-terminal helix-turn-helix domain (HTH; InterPro IPR000047) characteristic of DNA-binding proteins[22] (Supplementary Fig. 16). These two domains are required for the function of RocS in chromosome segregation as both ΔHTH-rocS and rocS-ΔAH R800 cells displayed growth and viability defects, as well as an anucleate phenotype and cell shapes similar to ΔrocS R800 cells (Fig. 3c and Supplementary Fig. 17). In addition, deletion of either the AH or the HTH domain drastically altered the localization pattern of RocS (Fig. 3c,d). The deletion of the N-terminal HTH domain resulted in the discontinuous redistribution of GFP-ΔHTH-RocS at the cell periphery. Conversely, GFP-RocS-ΔAH colocalizes with the nucleoid in the pneumococcal cell (median $R = 0.85$, interquartile range $= 0.83–0.92$) (Fig. 3d), suggesting that RocS binds to DNA via the HTH domain. Chromatin immunoprecipitation sequencing (ChIP-seq) experiments (Supplementary Fig. 18) using a FLAG-RocS fusion protein (Supplementary Fig. 12) did not reveal any specific conserved DNA sequence targeted by RocS. We further showed that DNA binding was independent of the size, GC content and sequence of the DNA fragment (Supplementary Fig. 19a,b). Interestingly, analysis of the HTH domain of RocS indicates that it resembles that of regulators of the Lrp and MarR families[22]. Some members of these families, such as LrpC from *Bacillus subtilis*, bind intrinsically to curved sequences of DNA[23]. Thus, RocS may recognize some topological features of the DNA. Finally, to confirm that the HTH domain of RocS is required and sufficient for DNA binding, we substituted the highly conserved glycine 15 residue of the HTH domain with a proline residue[22] (Supplementary Fig. 16) and showed that DNA binding of RocS-G15P-ΔAH was nearly completely abolished (Supplementary Fig. 19c). Collectively, these data show that the C-terminal AH domain is required for the interaction of RocS with the membrane, whereas the N-terminal HTH domain mediates RocS DNA binding; both domains are essential for RocS function.

We finally questioned the biological role of the interaction between RocS and the tyrosine-autokinase CpsD (Supplementary Fig. 1). Previous findings showed that CpsD possesses a structural fold comparable to that of ParA proteins that usually assist ParB in chromosome segregation[10,24,25]. As ParA is absent in the pneumococcus[7] and CpsD interacts directly with ParB, it was proposed that CpsD could act as a ParA-like protein[10]. Interestingly, this interaction is modulated by the autophosphorylation of CpsD, and mimicking permanent phosphorylation of CpsD (CpsD-3YE) promotes capsule biogenesis and normal chromosome segregation by enabling ParB mobility[10] (Fig. 4a). By contrast, defective autophosphorylation of CpsD (CpsD-3YF) not only impairs capsule production but also reduces ParB mobility, inducing aberrant chromosome segregation and leading to cell elongation[10] (Fig. 4b). As a consequence, even in the absence of a conserved nucleoid occlusion system in the pneumococcus[7], cell division appears to
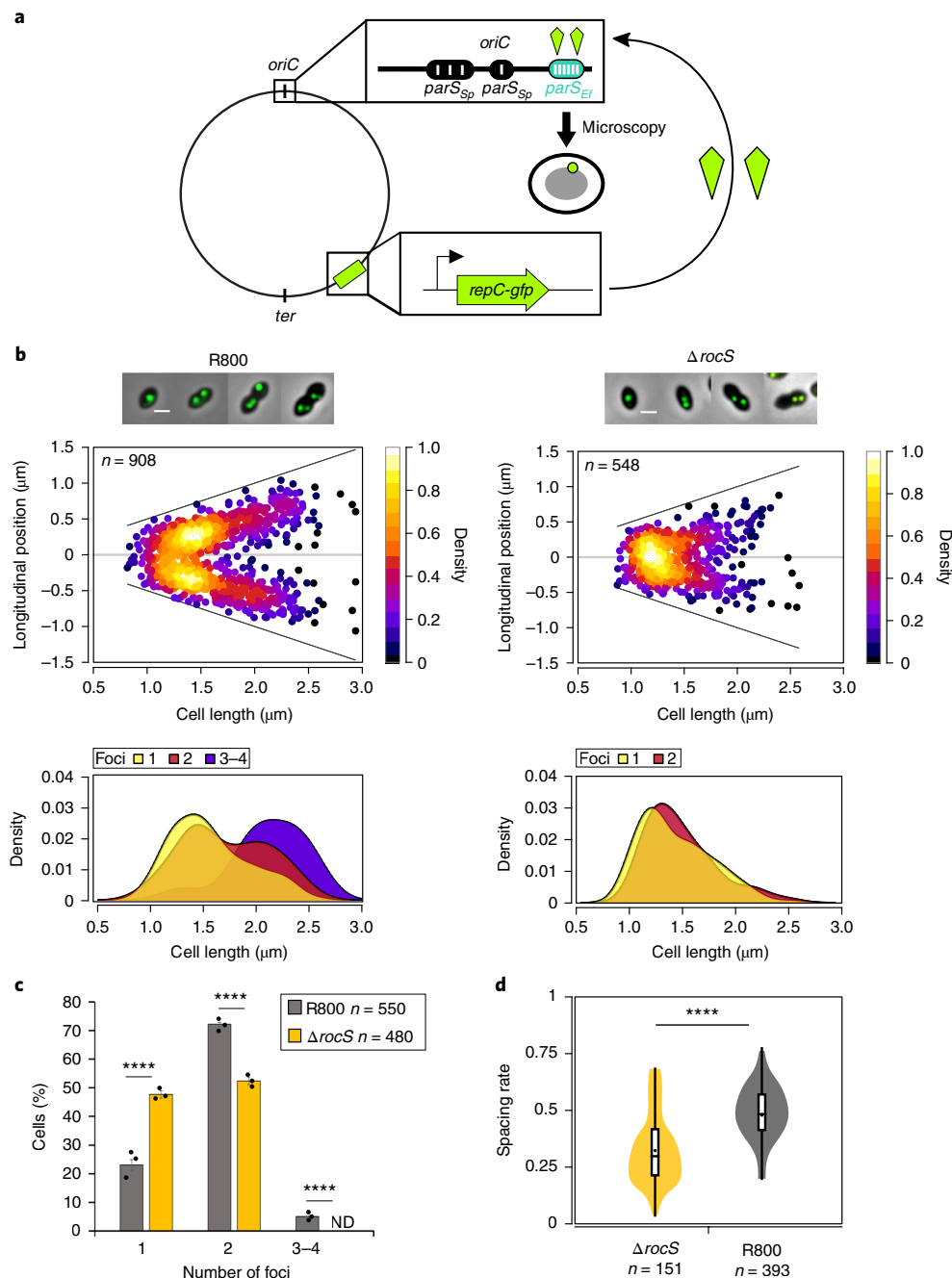
Fig. 2 | *oriC* segregation patterns in WT and Δ*rocS* cells. a, Schematic representation of the Par system used to image *oriC*. *parS* sequences from *E. faecalis* (*parS_Ef*, blue oval) were inserted into the chromosome near the pneumococcal *oriC* while the *parB* homologue *repC* fused to *gfp* (*repC-gfp*) is expressed ectopically under the control of the P_{comX} promoter. On loading of *repC-gfp* onto *parS_Ef* sites, the localization of *oriC* is followed by fluorescence microscopy (green dot). *parS_Sp* indicates native pneumococcal *parS* sites. **b**, In the upper panels localization heat maps of *oriC* (RepC-GFP) positions along the cell length in WT and Δ*rocS* R800 cells are shown. Representative merged images between phase-contrast and GFP fluorescence signals of cells with either 1, 2 or 3/4 foci are shown on the top. In the lower panels, Kernel density plots of the cell length in relation to the number of foci in WT and Δ*rocS* R800 cells are shown. Upper and lower diagonal lines indicate the position of the cell poles. The grey line indicates mid-cell. Scale bars, 1 μm. **c**, Relative percentages of cells as a function of the number of *oriC* foci in R800 WT and Δ*rocS* cells. The bars, with data points overlapping, represent the mean ± s.e.m. Two-tailed *P* values were derived from a two-population proportion test for the following pairs of proportions: R800-WT versus R800-Δ*rocS* 1 foci ($P < 0.0001$), 2 foci ($P = 8.9 \times 10^{-16}$) and 3 foci ($P = 1.5 \times 10^{-10}$). **d**, Measurements of the spacing rate (the relative distance between two foci of *oriC* in relation to the cell length). The box indicates the 25th to the 75th percentile and the whiskers indicate the minimum and the maximum values. The mean and the median are indicated with a dot and a line in the box, respectively. The two-tailed *P* value was derived from a Mann–Whitney test between R800-WT and R800-Δ*rocS* ($P = 7.9 \times 10^{-9}$). ****$P < 0.0001$. *n* indicates the number of cells analysed. Experiments were performed in triplicate.

be blocked to protect the nucleoid against truncation by the newly forming septum when CpsD is not phosphorylated. To test whether RocS could be involved in this process, we deleted *rocS* in D39

strains mimicking either permanent or defective phosphorylation of CpsD (Δ*rocS-cpsD-3YE* and Δ*rocS-cpsD-3YF*, respectively) and looked at the cell morphology, capsule production and DNA
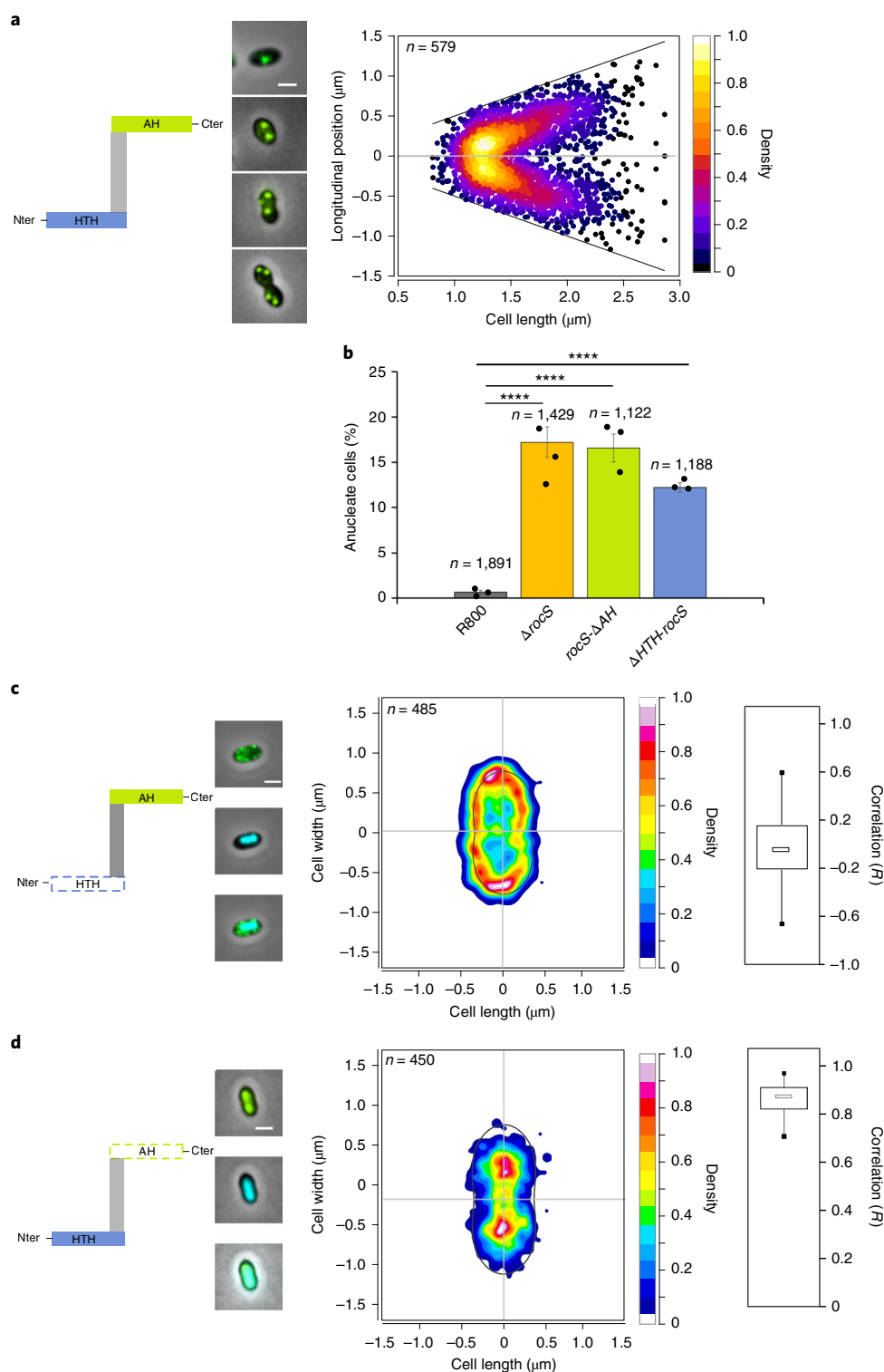
Fig. 3 | Localization of GFP-RocS and derivatives and the effect on nucleoid localization. Schematic representations of RocS and derivatives are shown on the left of panels **a**, **c** and **d**. Cter, C terminal; Nter, N terminal. **a**, Heat map representing the longitudinal localization of GFP-RocS as a function of the cell length in R800 cells (right). Upper and lower diagonal lines indicate the position of the cell poles. The grey line indicates mid-cell. Representative merged images of cells with either one, two, or three or four foci are also shown (middle). Scale bar, 1 μm. **b**, Relative percentage of anucleate cells for *rocS*-ΔAH and Δ*HTH-rocS* R800 strains. The bars, with data points overlapping, represent the mean ± s.e.m. *n* indicates the total number of cells analysed from three independent experiments. The two-tailed *P* values were derived from a two-population proportion test for the following pairs of proportions: R800-WT versus R800-Δ*rocS* ($P < 0.0001$), R800-WT versus R800-*rocS*-ΔAH ($P < 0.0001$) and R800-WT versus R800-Δ*HTH-rocS* ($P < 0.0001$). ****$P < 0.0001$. **c,d**, Heat maps representing the two-dimensional localization patterns of GFP-ΔHTH-RocS (**c**) and GFP-RocS-ΔAH (**d**) in R800 cells. Representative overlays of phase contrasts and GFP or DAPI fluorescence signals, or both signals, are shown on the left. Scale bars, 1 μm. The distribution of the Pearson correlation coefficient (*R*), measured between the DAPI and GFP signals for each strain are shown as box (the 25th to the 75th percentile) and whisker (minimum and maximum values) plots on the right.
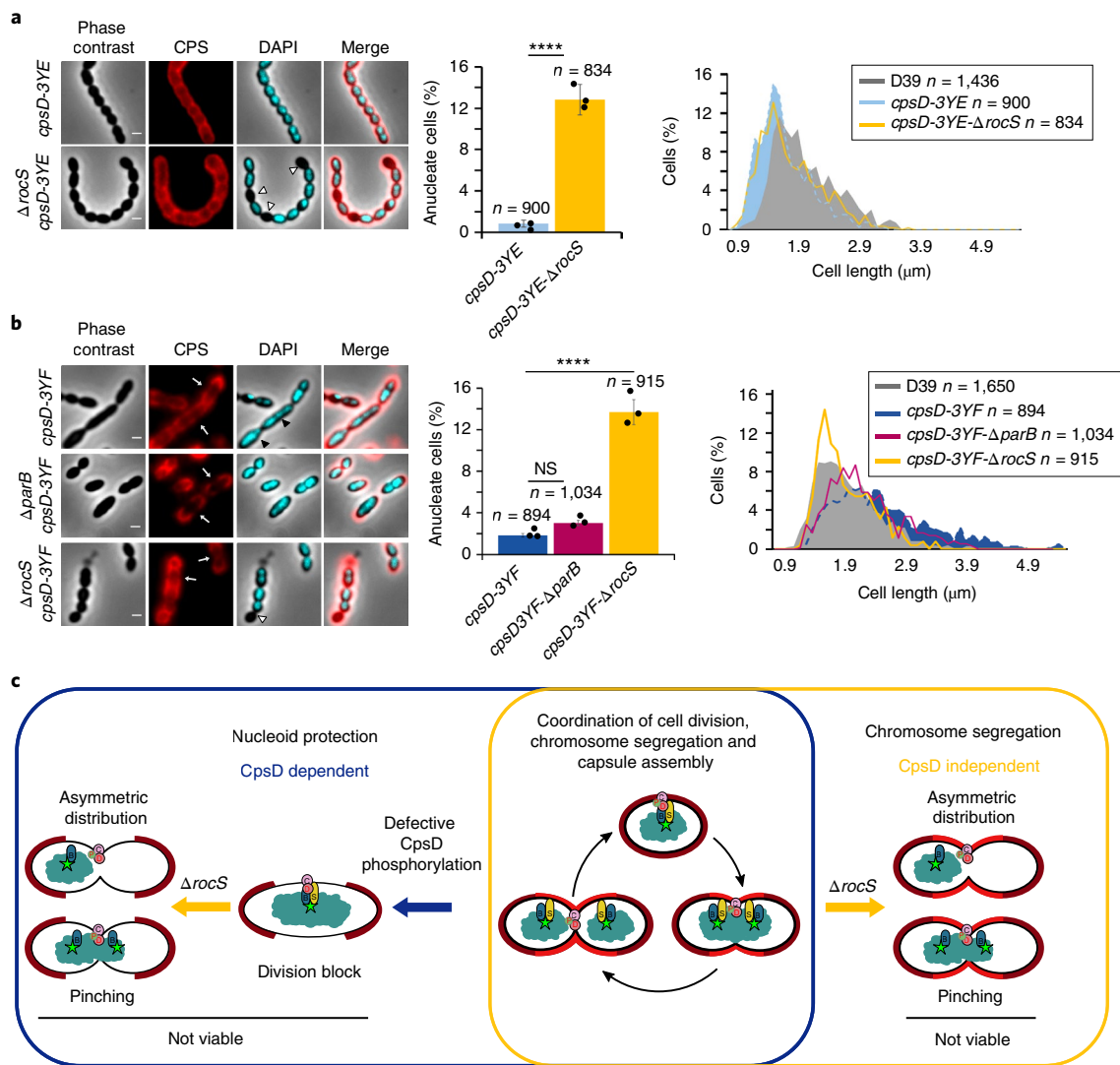
Fig. 4 | Deletion of *rocS* in phospho-ablative and phospho-mimetic CpsD mutants and a model for the RocS nucleoid protection system. a,b, Detection of CPS and DNA in *cpsD-3YE* and *cpsD-3YE-ΔrocS* (**a**) and *cpsD-3YF*, *cpsD-3YF-ΔparB* and *cpsD-3YF-ΔrocS* (**b**). Phase-contrast, CPS, DAPI and merged images are shown on the left. The white arrows indicate CPS production defects, the white arrowheads show anucleate cells and the black arrowheads indicate nucleoid segregation defects. Scale bars, 1 μm. The corresponding percentage of anucleate cells are shown as bar charts (middle). The bars, with data points overlapping, represent the mean ± s.e.m. Two-tailed *P* values were derived from a two-population proportion test for the following pairs of proportions: *cpsD-3YE* versus *cpsD-3YE-ΔrocS* ($P < 0.0001$), *cpsD-3YF* versus *cpsD-3YF-ΔrocS* ($P = 1.9 \times 10^{-13}$) and *cpsD-3YF* versus *cpsD-3YF-ΔparB* ($P = 1.2$). $****P < 0.0001$. The corresponding distribution of the cell length is shown on the right as histograms. *n* indicates the number of cells analysed from three independent experiments, and standard errors are indicated with error bars. **c,** Model for the nucleoid protection system coordinating capsule synthesis, chromosome segregation and cell division. Non-phosphorylated CpsD hinders both capsule synthesis and chromosome segregation, inducing a division block. The deletion of *rocS* alleviates the division block and results in uncontrolled cell constriction with improper chromosome segregation (pinching and asymmetric distribution), leading to non-viable progeny. ParB, RocS, CpsD and its transmembrane activator CpsC are indicated by blue, yellow, red and pink circles, respectively. The red 'P' and the green star indicate CpsD autophosphorylation and the *oriC* region, respectively. Capsule is shown in light (new capsule produced during cell division) and dark (inherited from the mother cell) red.

content. As expected, the deletion of *rocS* generated approximately 13% of anucleate cells in both cases (Fig. 4). Strikingly, while the deletion of *rocS* in the permanent phosphorylation *cpsD-3YE* mutant did not affect the cell morphology, the deletion of *rocS* suppressed the elongated phenotype of the defective phosphorylation *cpsD-3YF* mutant (Fig. 4). This property is specific to *rocS*, as the deletion of *parB* in the defective phosphorylation *cpsD-3YF* mutant strain had only a modest effect on cell elongation (Fig. 4b). By contrast, overproducing RocS in the absence of CpsD also induced an elongated phenotype (Supplementary Fig. 20). This suggests that, although the division block depends on the phosphorylation state of CpsD, the latter can be bypassed by overexpression of *rocS*. As a

result, RocS, along with the CpsD phosphorylation level, blocks cell division to protect the nucleoid against truncation.

To get more insight into the interplay between RocS and CpsD, we looked at the colocalization between CpsD-mKate2 and GFP-RocS in D39 cells. As expected, because CpsD localized exclusively at mid-cell throughout the cell cycle[10], RocS colocalized with CpsD only at the early stage of the cell cycle (Supplementary Fig. 21). As RocS migrates with *oriC* and thus with the nucleoid as the cell elongates, one can assume that RocS and CpsD can interact only when the nucleoid is not fully or properly segregated. Thus, both the phosphorylation state of CpsD and the co-occurrence of RocS and CpsD at mid-cell could regulate the constriction and eventually block cell

division when the nucleoid is not properly segregated. Interestingly, we found that RocS interacts with FtsZ in vitro (Supplementary Fig. 22), suggesting that this cell division block could result from a direct action of RocS on the Z-ring.

Our results suggest that RocS has two main roles during the pneumococcal cell cycle: (1) RocS, independently of CpsD, is required for proper chromosome partitioning, and (2) RocS, along with CpsD, regulate constriction and eventually blocks cell division to ensure proper capsule secretion and to protect the nucleoid against premature truncation (Fig. 4c). Typical nucleoid occlusion systems prevent the assembly of the FtsZ ring over the nucleoid[26,27]. However, FtsZ rings were found to be properly positioned at the division septum in *cpsD-3YF* elongated cells[10], indicating that the constriction rather than the assembly of the FtsZ ring at mid-cell was blocked by RocS. Thus, RocS constitutes an authentic nucleoid protection system, which is mechanistically distinct from the typical nucleoid occlusion mechanisms. Cell elongation of the pneumococcus is not achieved by MreB-mediated lateral insertion of peptidoglycan, but rather organized by the Z-ring itself at the cell centre[28]. Preventing the assembly of the Z-ring over the nucleoid, like in rod-shaped bacteria, would thus hinder cell elongation and therefore the cell division of the pneumococcus. The latter, and probably all Streptococcaceae (Supplementary Fig. 2), have therefore evolved their own nucleoid protection system to avoid premature truncation of the nucleoid during cell division. Overall, our work demonstrates that RocS can be viewed as the cornerstone of a process connecting and coordinating capsule synthesis, chromosome segregation and cell division. The 'raison d'être' of such a regulatory process coordinating capsule synthesis with cell cycle progression is likely to make sure that cells are covered by capsule at every step of the cell cycle to prevent detection by the human immune system.

Methods

Strains and growth conditions. The strains used in this study are listed in Supplementary Table 1. *S. pneumoniae* R800, D39Δcps[29] and D39 and derivatives were cultivated at 37 °C in C+Y medium or THY broth at pH 7.4.

Cell growth curves were monitored in the JASCO V-630-BIO-spectrophotometer and the optical density (OD) was read automatically every 10 min. The *E. coli* XL1-B strain[30] was used for cloning, and the *E. coli* BL21 strain[31] was used for overproduction of CpsC/D, RocS, RocS-ΔAH, ParB and FtsZ. *E. coli* strains were grown in LB supplemented with appropriate antibiotic. Growth was monitored by OD readings at 550 nm or 600 nm for *S. pneumoniae* or *E. coli* strains, respectively.

Construction of plasmids and strains. Gene modifications (*gfp*, *mkate2* and *flag* fusions, knockout and domain deletion) in *S. pneumoniae* were achieved by homologous recombination using the two-step procedure based on a bicistronic *kan-rpsL* cassette called Janus[32] and constructed at their native chromosomal locus. Thus, they are expressed under the control of the native promoter and represent the only source of the protein.

Δ*rocS* D39, Δ*rocS* R800, Δ*rocS-Δsmc* R800 and Δ*rocS-ΔparB* R800 strains were complemented ectopically for *rocS* expression using the strategy described in ref. [33] using the competence inducible system of *Streptococcus thermophilus*. The ComS-inducible *comR* DNA fragment was introduced between the *treR* and *amiF* loci of both strains. Then, the *rocS* copy under the control of the *comX* promoter was inserted between the *cpsN* and *cpsO* genes in R800 or at the *bgaA* locus in D39 strains.

For constructing the system for tagging *ori*, we used the *parS* sites and the ParB homologue RepC-GFP from *E. faecalis*[19]. The *parS* sites were inserted between *thmA* and IS1167 loci near the pneumococcal origin of replication. Then, *repC-gfp* under the control of the promoter of the *comX* gene of *S. thermophilus* was used for PCR and inserted between the *cpsN* and *cpsO* genes in the R800 strain. *repC-gfp* expression was induced with 1 μM ComS.

To construct the thermosensitive *dnaA* R800 mutated strain, we PCR amplified the *dnaA(T1193C)* mutated gene of the D39 thermosensitive mutant described in Kjos et al.[16]. The DNA fragment was then transformed in the R800 strain and cells were plated at 30 °C. After overnight growth, colonies were resuspended in THY broth and cultured again on plates at either 30 °C or 40 °C. The mutation in *dnaA* was checked by DNA sequencing in clones growing at 30 °C but not at 40 °C.

For the construction of plasmids overproducing RocS-ΔAH-6His or native FtsZ, we PCR amplified DNA fragments encoding either RocS from Met 1 to Gln 150 or FtsZ from Met 1 to Arg 419, respectively, using chromosomal DNA from the *S. pneumoniae* R800 strain as a template. The obtained *rocS* or *ftsZ* DNA fragments were cloned into either the *NdeI* and *PstI* or the *NdeI* and *HindIII* cloning sites of pT7-7 (ref. [34]). Site-directed mutagenesis of glycine 15 to proline of RocS was performed by PCR using the plasmid pT7.7-rocSΔAH (Supplementary Table 1) as a template. The other plasmids used in this study are described in Supplementary Table 1.

The oligonucleotides used for all constructions are listed in Supplementary Table 2. Plasmids and pneumococcal strains were verified by DNA sequencing to verify error-free PCR amplification.

Protein purification. Purification of the chimaera 6His-CpsC/D and ParB-6His was performed as described previously[10]. To purify RocS-ΔAH-6His, *E. coli* BL21 strains were used and cultured at 37 °C in LB medium. At OD$_{600}$ = 0.6, 1 mM IPTG (isopropyl-β-D-thiogalactoside) was added and the culturing of cells were continued for 3 h at 37 °C. Cells were then harvested by centrifugation and resuspended in buffer A (25 mM Tris-HCl, pH 7.5, 1 M NaCl, 10 mM imidazole and 10% glycerol) containing 10 mg ml⁻¹ lysozyme and 1 μg ml⁻¹ protease inhibitor (Roche Diagnostics). After sonication and centrifugation, the supernatant was loaded on to a Ni-NTA agarose resin (Qiagen) and extensively washed with buffer A containing 20 mM imidazole. RocS-6His was eluted with buffer B (25 mM Tris-HCl, pH 7.5, 300 mM NaCl, 300 mM imidazole and 10% glycerol). Pure fractions were pooled and dialysed against buffer C (50 mM HEPES, pH 7.5, or 25 mM Tris, pH 7.5, 150 mM NaCl and 10% glycerol).

To purify FtsZ, *E. coli* BL21 strains were used and cultured at 37 °C in LB medium. At OD$_{600}$ = 0.6, 1 mM IPTG was added and the culturing of cells were continued for 2 h at 37 °C. Cells were then harvested by centrifugation and resuspended in buffer D (50 mM Tris-HCl, pH 8, 50 mM KCl and 1 mM EDTA) containing 10 mg ml⁻¹ lysozyme, 1 μg ml⁻¹ protease inhibitor (Roche Diagnostics) and 1 μg ml⁻¹ DNase-RNase (Sigma). After sonication and centrifugation, ammonium sulfate was added to the supernatant at 4 °C to a final concentration of 30% and stirred for 30 min. The mixture was then centrifuged at 25,000*g* for 30 min, and the pellet was retained, resuspended in buffer D and the solution was dialysed against buffer D for 4 h at 4 °C. The supernatant was then applied to a HiTrap Q HP column (GE Healthcare). After extensive washing, the protein was eluted with a gradient of 0–50% of buffer E (buffer D + 1 M KCl). Peak fractions containing FtsZ were pooled and concentrated in Amicon filters (10 kDa cut-off). The concentrated lysate was further injected into a GE-Hiload 16/600 superdex 200 size-exclusion chromatography column. The FtsZ protein peaks were collected in buffer D and analysed on SDS–PAGE. Homogenous fractions were collected and concentrated as mentioned above. The final buffer was 50 mM Tris-HCl pH 8, 200 mM KCl, 1 mM EDTA and 10% glycerol.

Protein concentrations were determined using a Coomassie assay protein dosage reagent (Uptima), and proteins were then aliquoted and frozen at −80 °C.

Co-immunoprecipitation and immunoblot analysis. For co-immunoprecipitation, cultures of *S. pneumoniae* cells were grown at 37 °C in C+Y medium until OD$_{550}$ = 0.3. Cell pellets were incubated at 30 °C for 30 min in buffer A (0.1 M Tris-HCl, pH 7.5, 2 mM MgCl$_2$, 1 M sucrose, 6 mg ml⁻¹ DNase I and RNase A, and 1 μg ml⁻¹ protease inhibitor). After centrifugation at 4 °C, the pellet was resuspended in buffer B (0.1 M Tris-HCl, pH 7.5, 1 mM EDTA, 0.1% Triton X-100, 6 mg ml⁻¹ of DNase I and RNase A, and 1 μg ml⁻¹ protease inhibitor) and incubated for 15 min at room temperature before being harvested by centrifugation. The supernatant was then incubated with Dynabeads (Invitrogen) coupled with 20 μg anti-FLAG or anti-GFP antibodies and incubated for 2 h at 4 °C. After extensive washing with buffer C (10 mM Tris-HCl, pH 7.5, 0.5 mM EDTA, 0.1% Triton X-100, 150 mM NaCl and 1 μg ml⁻¹ of protease inhibitor), protein-bound beads were eluted with SDS–PAGE loading buffer at 95 °C for 10 min and analysed by SDS–PAGE and immunoblotting using either a rabbit anti-GFP antibody at 1/10,000 (AMS Biotechnology), the anti-FLAG antibody at 1/1,000 (Sigma) or the anti-mKate2 antibody at 1/3,000 (Invitrogen).

For immunoblot analysis, *S. pneumoniae* cells were resuspended in TE buffer (25 mM Tris-HCl, pH 7.5, and 1 mM EDTA) supplemented with protease and phosphatase inhibitor cocktail II (Sigma-Aldrich) and lysed by sonication. Crude extracts (25 μg) were analysed by SDS–PAGE, electrotransferred onto a polyvinylidene difluoride membrane and incubated with either rabbit anti-RocS antibody at 1/5,000 (produced by Eurogentec with purified RocS-ΔAH-6His), rabbit anti-enolase polyclonal antibody at 1/500,000 (ref. [35]) or rabbit anti-serotype 2 capsular polysaccharide (CPS) polyclonal antibody at 1/2,000 (Statens Serum Institute). A horseradish peroxidase-conjugated goat anti-rabbit polyclonal antibody (Bio-Rad) was used at 1/5,000 to reveal immunoblots.

Yeast two-hybrid. The yeast two-hybrid genetic screens were carried out using a mating strategy as described previously[14,36]. Construction of the pGBDU-cpsD and pGBDU-cpsC bait plasmids and expressing CpsD fused to the DNA binding domain (BD) of Gal4 was described in ref. [10]. This plasmid was introduced in the PJ69-4(α) haploid strain. This strain was then mated with a PJ69-4 haploid(α) strain harbouring a library of pGAD plasmids expressing genomic fragments of *S. pneumoniae* R6 in fusion with the Gal4 activating domain (AD)[14]. Potential binary interactions were selected by the ability of the yeast diploids to grow on

synthetic media agar SC–LUH lacking leucine (L) and uracil (U) to select for maintenance of the plasmids pGAD and pGBDU, respectively, as well as histidine (H), to select for the interaction[37]. In addition, binary interactions were tested by a matrix-based approach by mating haploid cells expressing BD-CpsD with haploid cells of complementary mating type expressing the AD-prey protein fusions RocS[50–163], RocS, CpsC and CpsD. Diploids were first selected onto –LU media and further tested for interacting phenotypes (that is, the ability to grow on SC–LUH selective agar plates) to reveal binary interactions between bait and prey proteins.

Preparation and analysis of CPS. CPS were prepared as previously described[10]. Briefly, *S. pneumoniae* cultures were grown until $OD_{550} = 0.3$, washed once with PBS and resuspended in buffer A (50 nM Tris-HCl, pH 7.4, 20% sucrose and 50 nM $MgSO_4$). The solution was then supplemented with 400 units of mutanolysin and $6\,\mu g\,\mu l^{-1}$ DNase and RNase and incubated overnight at room temperature. After centrifugation at $16,000g$ for 20 min at 4 °C, pellets were resuspended in the same volume of buffer A. Of the mixture, 10 μl were then mixed with 5 μl buffer B (50 mM Tris-HCl, pH 8.0, 50 mM EDTA, 0.5% Tween-20 and 0.5% Triton X-100) and 20 μg proteinase K, incubated for 30 min at 37 °C and analysed by SDS–PAGE and immunoblotting.

Microscopy techniques. Cells were grown until $OD_{550} = 0.1$. For immunofluorescence microscopy, cells were mixed with the rabbit serotype 2 CPS polyclonal antibody (Statens Serum Institute) at 1/1,000, washed and then incubated with the anti-rabbit Dylight-549 antibody (Jackson ImmunoResearch) at 1/2,000. After a last wash with PBS, CPSs were imaged and the fluorescence intensity was measured as described previously[10].

For 4,6-diamidino-2-phenylindole (DAPI) staining, 10 μl *S. pneumoniae* cell culture were mixed with 1 μl DAPI at $2\,\mu g\,\mu l^{-1}$ (Molecular Probes) and incubated for 5 min at room temperature. For mKate2 and GFP fluorescence imaging, cells were spotted on pads made of 1.5% agarose in C+Y medium at 37 °C as previously described[38].

Slides were visualized with a Nikon TiE microscope fitted with an Orca-CMOS Flash4 V2 camera with a 100×1.45 objective. Images were collected using NIS-Elements (Nikon). For total internal reflection fluorescence experiments, data acquisition was done every 100 ms to 2 s. Images were analysed using the software ImageJ (http://rsb.info.nih.gov/ij/) and the plugin MicrobeJ[39].

Diffraction-limited foci of RepC-GFP or GFP-RocS were detected using the feature/spot detection option in MicrobeJ. This option combines spatial 2D filtering (Median Filter) and a 2D local maxima algorithm to localize single fluorescent maxima in each detected cell. Each maximum was then fit to a single-peak or a multi-peak 2D Gaussian curve, to determine their amplitude, their full width at half maximum and their coordinates at the subpixel resolution. Maxima were finally filtered based on the goodness of the fit and their amplitude. Their subcellular localizations were automatically computed for each associated particle.

Microscale thermophoretic analysis. Microscale thermophoresis[40] was used to test the interaction of RocS-AH with the chimaera CpsC/D, ParB and FtsZ. Binding experiments were carried out with a Monolith NT.115 Series instrument (Nano Temper Technologies). RocS-ΔAH was labelled with the red dye NT-647. Briefly, a sample containing 50 nM of labelled RocS-ΔAH-6His, and increasing concentrations of 6His-CpsC/D (from 275 pM to 9 μM), ParB-6His (from 427 pM to 14 μM) or FtsZ (from 686 pM to 22.5 μM) were loaded onto K023 Monolith NT.115 hydrophobic capillaries and thermophoresis was measured for 30 s at 25 °C. Each measurement was made in triplicate. Experiments were carried out at 25 °C in 10 mM HEPES, pH 7.5, 150 mM NaCl and 0.05% Tween-20. Analysis was performed with the Monolith software. The dissociation constant (K_d) to measure affinity was quantified by analysing the change in normalized fluorescence (FNorm = fluorescence after thermophoresis/initial fluorescence) as a function of the concentration of the titrated 6His-CpsC/D or ParB-6His proteins.

***oriC/ter* ratio determination by real-time quantitative PCR.** Genomic DNA was extracted using the DNA Maxima Kit (Qiagen). Real-time quantitative PCR was performed as described previously[18]. Briefly, each 20 μl sample comprised 8.8 ng DNA, 0.6 pmol of each primer (Supplementary Table 2) and 10 μl of the 2× SYBR Green Supermix (Bio-Rad). Amplification was performed on an iQ5 Real-Time PCR Detection System (Bio-Rad). To find amplification efficiencies, Monte Carlo simulations were performed in R. Average Ct (cycle threshold) values and their corresponding standard deviations were used to simulate 10,000 new sets of Ct values that were used to compute the amplification efficiencies for each set. From that population of possible efficiencies, averages and standard deviations were derived. Analysis of the real-time quantitative PCR experiments for *oriC/ter* ratio determination was performed using the $2^{-\Delta\Delta CT}$ method[41], with the important difference that the earlier-found amplification efficiencies were used to determine the fold change per cycle, instead of assuming it to equal 2. As a reference, cells with an assumed *oriC/ter* ratio of 1 were used. For that, a thermosensitive *dnaA* mutant (*dnaA-T1193C*) was grown at 30 °C until an OD_{600} of 0.05. Then, cells were transferred to non-permissive temperature (40 °C) and incubated for 1 h, followed by harvesting and isolation of chromosomal DNA. Uncertainties in *oriC/ter* ratios were also determined by Monte Carlo simulations.

Bioinformatic analyses. For the phylogenetic analysis, homologues of RocS were retrieved using iterative BLASTP from BLAST package 2.2.6 against a local database containing 4,466 prokaryotic complete proteomes retrieved from NCBI ftp (ftp://ftp.ncbi.nlm.nih.gov/). The Spr0895 amino acid sequence (NP_358489.1) was used as the first seed. Protein sequences detected as homologues were aligned with MAFFT v7.123b[42] and used to build an HMM profile with HMMER v3.1b1 (ref. [43]). The profile was then used to query the local database with HMMSEARCH from the HMMER package. Plasmid sequences were removed from the analysis. The phylogeny of Lactobacillales has been inferred from a supermatrix of ribosomal proteins. One strain per family was selected to represent each family in Lactobacillales and a sequence of one species of Listeriaceae was added to root the tree. The sequences were aligned using MAFFT (L-INS-I option) and trimmed with BMGE-1.1 (option BLOSUM30)[44]. The evolution model was chosen using Bayesian Information criteria and the phylogeny was inferred using PhyML[45] (LG + I + F + G4, 8 sequences, 6,219 positions).

Secondary structure predictions of RocS were obtained using PSIPRED[46]. The helical representation of RocS and MinD of *E. coli* was made using http://www.tcdb.org/progs/?tool=pepwheel.

ChIP-seq and data analysis. The protocol for immunoprecipitation of FLAG-tagged RocS was largely performed as described by Minnen et al.[8] and was performed in duplicate. Specifically, cells were pre-cultured in acid C+Y (pH 6.8) and grown until $OD_{600} = 0.2$. Cells were then diluted 1:50 in acid C+Y, to a final volume of 250 ml and grown until $OD_{600} = 0.20$. Then, 25 ml fixation buffer (11% formaldehyde, 5 mM NaOH, 50 mM Tris, pH 8.0, 100 mM NaCl, 0.5 mM EGTA and 1 mM EDTA) was added, the culture was mixed by inversion and incubated at room temperature for 30 min. Formaldehyde was quenched by the addition of 92 ml of 1 M Tris, pH 8, and 10 min of incubation at room temperature. First, cells were spun down at 5,000g for 12 min at 4 °C and washed in 20 ml ice-cold PBS. Second, cells were spun down at 5,000g for 12 min at 4 °C and washed in 10 ml ice-cold PBS. Third, cells were spun down at 5,000g for 12 min at 4 °C and washed in 1 ml ice-cold PBS. Finally, cells were spun down at 11,000g for 2 min at 4 °C, supernatant was removed and the pellet was snap-frozen in liquid nitrogen and stored at −80 °C.

Dynabeads Protein G (Invitrogen) were prepared according to the manufacturer's instructions and loaded with 10 μg anti-FLAG antibody. Cell pellets were resuspended in 2 ml ice-cold lysis buffer (50 mM HEPES-KOH, pH 7.55, 140 mM NaCl, 1 mM EDTA, 1% Triton X-100, 0.1% sodium deoxycholate, 1 mM phenylmethylsulfonyl fluoride, protease inhibitor cocktail and 100 mg ml⁻¹ RNase) and transferred to a 5-ml round-bottom tube. Samples were sonicated on ice two times for 10×30 s on a Sonics Vibracell VCX130 with 65% amplitude. Samples were then split into 200 μl whole-cell extract (stored at −20 °C) and 800 μl for immunoprecipitation. The latter fractions were incubated for 2–4 h at 4 °C on a rotating wheel. Supernatant was removed on a magnet. The beads were washed three times for 5 min, shaking at 800 r.p.m. at room temperature. The first wash was performed with 1 ml lysis buffer, the second wash with 1 ml lysis buffer with extra NaCl (500 mM final concentration) and the third wash with 1 ml wash buffer (10 mM Tris, pH 8.0, 250 mM LiCl, 1 mM EDTA, 0.5% NP-40, 0.5% sodium deoxycholate and 1 mM phenylmethylsulfonyl fluoride). Supernatant was removed and beads were resuspended in 520 μl TES buffer. Whole-cell extract samples were thawed and combined with 300 μl TES buffer and 20 μl of 10% SDS. To elute DNA, both whole-cell extracts and immunoprecipitates were incubated overnight on a shaker at 65 °C. On a magnet, the DNA-containing supernatant was transferred to a fresh tube.

To the DNA samples, 1 μl phenol per μl of sample was added, followed by vortexing and centrifugation at 11,000g for 5 min. The DNA-containing layer was then added to 1 μl chloroform per 1 μl of sample, followed by vortexing and centrifugation at 11,000g for 5 min. The DNA-containing layer was transferred to a fresh tube, and 1 μl of glycogen (Roche) and 40 μl of 3 M NaOAc (pH 5.3) were added. After mixing, 1 ml pure ethanol was added and tubes were incubated for 20 min at −20 °C, followed by centrifugation for 15 min at 4 °C. The pellets were resuspended in 100 μl TE (pH 8.0) and incubated for 15 min at 65 °C. DNA fragmentation was verified on an agarose gel.

GATC Biotech performed further library preparation and sequencing on an Illumina HiSeq with 50-nucleotide single-end reads. Owing to an insufficient amount of material in one of the immunoprecipitate samples, we collected data on two whole-cell extract samples and one immunoprecipitate sample.

Sequencing reads were mapped to the *S. pneumoniae* R6 genome using Bowtie2 (ref. [47]). Visualization and peak calling was performed with SeqMonk (https://www.bioinformatics.babraham.ac.uk/projects/seqmonk/). Although no significant enrichment was detected by SeqMonk, we selected the 6 most intense peaks and extracted the 500 nucleotides surrounding the respective maximums[48]. Motif enrichment analysis was then performed using MEME-ChIP (https://www.ncbi.nlm.nih.gov/pubmed/21486936).

Electrophoretic mobility shift assay. Electrophoretic mobility shift assays were carried out by incubating different concentrations of purified protein RocS-ΔAH-6His or RocS-G15P-ΔAH-6His (0, 5, 10 and 15 μM) with 50 ng DNA in the following buffer (500 mM Tris-HCl pH 8.8, and 50 mM $MgSO_4$). DNA fragments of different lengths and percentages of GC content were PCR amplified (pUC18,

gfp or genomic DNA of *Pseudomonas aeruginosa* PA7) using the primers listed in Supplementary Table 2. Reactions were incubated for 15 min at 37 °C before being loaded onto 1% agarose gels. Gels were stained with ethidium bromide and imaged with UV light.

Data availability
The data that support the findings of this study are available from the corresponding author on request. The ChIP-seq data were deposited at the NCBI Sequence Read Archive (accession number PRJNA511435) and Gene Expression Omnibus (accession number GSE129717).

References
1. Toro, E. & Shapiro, L. Bacterial chromosome organization and segregation. *Cold Spring Harb. Perspect. Biol.* **2**, a000349 (2010).
2. Reyes-Lamothe, R., Nicolas, E. & Sherratt, D. J. Chromosome replication and segregation in bacteria. *Annu. Rev. Genet.* **46**, 121–143 (2012).
3. Wang, X., Montero Llopis, P. & Rudner, D. Z. Organization and segregation of bacterial chromosomes. *Nat. Rev. Genet.* **14**, 191–203 (2013).
4. Badrinarayanan, A., Le, T. B. & Laub, M. T. Bacterial chromosome organization and segregation. *Annu. Rev. Cell Dev. Biol.* **31**, 171–199 (2015).
5. Bohm, K. et al. Novel chromosome organization pattern in actinomycetales-overlapping replication cycles combined with diploidy. *mBio* **8**, e00511-17 (2017).
6. Grangeasse, C. Rewiring the pneumococcal cell cycle with serine/threonine- and tyrosine-kinases. *Trends Microbiol.* **24**, 713–724 (2016).
7. Pinho, M. G., Kjos, M. & Veening, J. W. How to get (a)round: mechanisms controlling growth and division of coccoid bacteria. *Nat. Rev. Microbiol.* **11**, 601–614 (2013).
8. Minnen, A., Attaiech, L., Thon, M., Gruber, S. & Veening, J. W. SMC is recruited to oriC by ParB and promotes chromosome segregation in *Streptococcus pneumoniae*. *Mol. Microbiol.* **81**, 676–688 (2011).
9. Grangeasse, C., Nessler, S. & Mijakovic, I. Bacterial tyrosine kinases: evolution, biological function and structural insights. *Phil. T. R. Soc. B* **367**, 2640–2655 (2012).
10. Nourikyan, J. et al. Autophosphorylation of the bacterial tyrosine-kinase CpsD connects capsule synthesis with the cell cycle in *Streptococcus pneumoniae*. *PLoS Genet.* **11**, e1005518 (2015).
11. Morona, J. K., Morona, R., Miller, D. C. & Paton, J. C. Mutational analysis of the carboxy-terminal (YGX)(4) repeat domain of CpsD, an autophosphorylating tyrosine kinase required for capsule biosynthesis in *Streptococcus pneumoniae*. *J. Bacteriol.* **185**, 3009–3019 (2003).
12. Yother, J. Capsules of *Streptococcus pneumoniae* and other bacteria: paradigms for polysaccharide biosynthesis and regulation. *Annu. Rev. Microbiol.* **65**, 563–581 (2011).
13. Henriques, M. X., Rodrigues, T., Carido, M., Ferreira, L. & Filipe, S. R. Synthesis of capsular polysaccharide at the division septum of *Streptococcus pneumoniae* is dependent on a bacterial tyrosine kinase. *Mol. Microbiol.* **82**, 515–534 (2011).
14. Mirouze, N., Claverys, J.-P. & Noirot, P. *Identification du Produit D'un Gène Tardif Impliqué dans la Régulation de la Compétence et dans le Processing de l'ADN lors de la Transformation Naturelle Chez* S. pneumoniae. PhD thesis, Paul Sabatier Univ. (2007).
15. Bechet, E. et al. Tyrosine-kinases in bacteria: from a matter of controversy to the status of key regulatory enzymes. *Amino Acids* **37**, 499–507 (2009).
16. Kjos, M. & Veening, J. W. Tracking of chromosome dynamics in live *Streptococcus pneumoniae* reveals that transcription promotes chromosome segregation. *Mol. Microbiol.* **91**, 1088–1105 (2014).
17. Yamanaka, K., Ogura, T., Niki, H. & Hiraga, S. Identification of two new genes, mukE and mukF, involved in chromosome partitioning in *Escherichia coli*. *Mol. Gen. Genet.* **250**, 241–251 (1996).
18. Slager, J., Kjos, M., Attaiech, L. & Veening, J. W. Antibiotic-induced replication stress triggers bacterial competence by increasing gene dosage near the origin. *Cell* **157**, 395–406 (2014).
19. Francia, M. V., Weaver, K. E., Goicoechea, P., Tille, P. & Clewell, D. B. Characterization of an active partition system for the *Enterococcus faecalis* pheromone-responding plasmid pAD1. *J. Bacteriol.* **189**, 8546–8555 (2007).
20. van Raaphorst, R., Kjos, M. & Veening, J. W. Chromosome segregation drives division site selection in *Streptococcus pneumoniae*. *Proc. Natl Acad. Sci. USA* **114**, E5959–E5968 (2017).
21. Zhou, H. & Lutkenhaus, J. Membrane binding by MinD involves insertion of hydrophobic residues within the C-terminal amphipathic helix into the bilayer. *J. Bacteriol.* **185**, 4326–4335 (2003).
22. Aravind, L., Anantharaman, V., Balaji, S., Babu, M. M. & Iyer, L. M. The many faces of the helix-turn-helix domain: transcription regulation and beyond. *FEMS Microbiol. Rev.* **29**, 231–262 (2005).
23. Tapias, A., Lopez, G. & Ayora, S. *Bacillus subtilis* LrpC is a sequence-independent DNA-binding and DNA-bending protein which bridges DNA. *Nucleic Acids Res.* **28**, 552–559 (2000).
24. Leipe, D. D., Wolf, Y. I., Koonin, E. V. & Aravind, L. Classification and evolution of P-loop GTPases and related ATPases. *J. Mol. Biol.* **317**, 41–72 (2002).
25. Gerdes, K., Howard, M. & Szardenings, F. Pushing and pulling in prokaryotic DNA segregation. *Cell* **141**, 927–942 (2010).
26. Wu, L. J. & Errington, J. Coordination of cell division and chromosome segregation by a nucleoid occlusion protein in *Bacillus subtilis*. *Cell* **117**, 915–925 (2004).
27. Bernhardt, T. G. & de Boer, P. A. SlmA, a nucleoid-associated, FtsZ binding protein required for blocking septal ring assembly over chromosomes in *E. coli*. *Mol. Cell* **18**, 555–564 (2005).
28. Fleurie, A. et al. Interplay of the serine/threonine-kinase StkP and the paralogs DivIVA and GpsB in pneumococcal cell elongation and division. *PLoS Genet.* **10**, e1004275 (2014).
29. Fenton, A. K., Mortaji, L. E., Lau, D. T., Rudner, D. Z. & Bernhardt, T. G. CozE is a member of the MreCD complex that directs cell elongation in *Streptococcus pneumoniae*. *Nat. Microbiol.* **2**, 16237 (2016).
30. Bullock, W. O., Fernandez, J. M. & Short, J. M. A high efficiency plasmid transforming recA *Escherichia coli* strain with β-galactosidase selection. *Biotechniques* **5**, 376 (1987).
31. Studier, F. W. & Moffatt, B. A. Use of bacteriophage T7 RNA polymerase to direct selective high-level expression of cloned genes. *J. Mol. Biol.* **189**, 113–130 (1986).
32. Sung, C. K., Li, H., Claverys, J. P. & Morrison, D. A. An rpsL cassette, janus, for gene replacement through negative selection in *Streptococcus pneumoniae*. *Appl. Environ. Microbiol.* **67**, 5190–5196 (2001).
33. Berg, K. H., Biornstad, T. J., Straume, D. & Havarstein, L. S. Peptide-regulated gene depletion system developed for use in *Streptococcus pneumoniae*. *J. Bacteriol.* **193**, 5207–5215 (2011).
34. Cortay, J. C. et al. In vitro asymmetric binding of the pleiotropic regulatory protein, FruR, to the ace operator controlling glyoxylate shunt enzyme synthesis. *J. Biol. Chem.* **269**, 14885–14891 (1994).
35. Fleurie, A. et al. Mutational dissection of the S/T-kinase StkP reveals crucial roles in cell division of *Streptococcus pneumoniae*. *Mol. Microbiol.* **83**, 746–758 (2012).
36. Marchadier, E. et al. An expanded protein-protein interaction network in *Bacillus subtilis* reveals a group of hubs: exploration by an integrative approach. *Proteomics* **11**, 2981–2991 (2011).
37. James, P., Halladay, J. & Craig, E. A. Genomic libraries and a host strain designed for highly efficient two-hybrid selection in yeast. *Genetics* **144**, 1425–1436 (1996).
38. de Jong, I. G., Beilharz, K., Kuipers, O. P. & Veening, J. W. Live cell imaging of *Bacillus subtilis* and *Streptococcus pneumoniae* using automated time-lapse microscopy. *J. Vis. Exp.* **28**, 3145 (2011).
39. Ducret, A., Quardokus, E. M. & Brun, Y. V. MicrobeJ, a tool for high throughput bacterial cell detection and quantitative analysis. *Nat. Microbiol.* **1**, 16077 (2016).
40. Jerabek-Willemsen, M., Wienken, C. J., Braun, D., Baaske, P. & Duhr, S. Molecular interaction studies using microscale thermophoresis. *Assay Drug Dev. Technol.* **9**, 342–353 (2011).
41. Livak, K. J. & Schmittgen, T. D. Analysis of relative gene expression data using real-time quantitative PCR and the $2^{-\Delta\Delta C_T}$ method. *Methods* **25**, 402–408 (2001).
42. Katoh, K. & Standley, D. M. MAFFT multiple sequence alignment software version 7: improvements in performance and usability. *Mol. Biol. Evol.* **30**, 772–780 (2013).
43. Eddy, S. R. A new generation of homology search tools based on probabilistic inference. *Genome Inf.* **23**, 205–211 (2009).
44. Criscuolo, A. & Gribaldo, S. BMGE (block mapping and gathering with entropy): a new software for selection of phylogenetic informative regions from multiple sequence alignments. *BMC Evol. Biol.* **10**, 210 (2010).
45. Guindon, S. et al. New algorithms and methods to estimate maximum-likelihood phylogenies: assessing the performance of PhyML 3.0. *Syst. Biol.* **59**, 307–321 (2010).
46. Jones, D. T. Protein secondary structure prediction based on position-specific scoring matrices. *J. Mol. Biol.* **292**, 195–202 (1999).
47. Langmead, B. & Salzberg, S. L. Fast gapped-read alignment with Bowtie 2. *Nat. Methods* **9**, 357–359 (2012).
48. Slager, J., Aprianto, R. & Veening, J. W. Deep genome annotation of the opportunistic human pathogen *Streptococcus pneumoniae* D39. *Nucleic Acids Res.* **46**, 9971–9989 (2018).

Author contributions

C.G. directed the study. C.M. conducted the cell imaging experiments and analyses with A.D., the genetic experiments with J.N., and the protein purification experiments and western blot analysis with J.-P.L., C.F. and S.N.N. C.M. and N.D. implemented the *oriC* localization system. J.-P.L. performed the microscale thermophoresis experiments. C.M. and J.S. performed the *oriC/ter* ratio and ChIP-seq experiments. M.-F.N.-G. performed the yeast two-hybrid experiments. P.S.G. performed the phylogeny analyses. All authors designed and analysed the data. C.G. and J.-W.V. wrote the manuscript and all authors edited the manuscript.

Competing interests

The authors declare no competing interests.

Additional information

Supplementary information is available for this paper at https://doi.org/10.1038/s41564-019-0472-z.

Reprints and permissions information is available at www.nature.com/reprints.

Correspondence and requests for materials should be addressed to C.G.

Publisher's note: Springer Nature remains neutral with regard to jurisdictional claims in published maps and institutional affiliations.

Corresponding author(s): Christophe Grangeasse

Reporting Summary

Nature Research wishes to improve the reproducibility of the work that we publish. This form provides structure for consistency and transparency in reporting. For further information on Nature Research policies, see Authors & Referees and the Editorial Policy Checklist.

Statistical parameters

When statistical analyses are reported, confirm that the following items are present in the relevant location (e.g. figure legend, table legend, main text, or Methods section).

n/a	Confirmed	
☐	☒	The exact sample size (*n*) for each experimental group/condition, given as a discrete number and unit of measurement
☐	☒	An indication of whether measurements were taken from distinct samples or whether the same sample was measured repeatedly
☐	☒	The statistical test(s) used AND whether they are one- or two-sided *Only common tests should be described solely by name; describe more complex techniques in the Methods section.*
☒	☐	A description of all covariates tested
☒	☐	A description of any assumptions or corrections, such as tests of normality and adjustment for multiple comparisons
☐	☒	A full description of the statistics including central tendency (e.g. means) or other basic estimates (e.g. regression coefficient) AND variation (e.g. standard deviation) or associated estimates of uncertainty (e.g. confidence intervals)
☐	☒	For null hypothesis testing, the test statistic (e.g. *F*, *t*, *r*) with confidence intervals, effect sizes, degrees of freedom and *P* value noted *Give P values as exact values whenever suitable.*
☐	☒	For Bayesian analysis, information on the choice of priors and Markov chain Monte Carlo settings
☒	☐	For hierarchical and complex designs, identification of the appropriate level for tests and full reporting of outcomes
☐	☒	Estimates of effect sizes (e.g. Cohen's *d*, Pearson's *r*), indicating how they were calculated
☐	☒	Clearly defined error bars *State explicitly what error bars represent (e.g. SD, SE, CI)*

Our web collection on statistics for biologists may be useful.

Software and code

Policy information about availability of computer code

Data collection	NIS-elements (Nikon) version 5.02
Data analysis	MicrobeJ (Ducret et al, 2016, Nat. Microbiol., 1, 16077) ImageJ (http://rsb.info.nih.gov/ij/) SeqMonk (https://www.bioinformatics.babraham.ac.uk/projects/seqmonk) MEME-ChIP (https:///www.ncbi.nlm.nih.gov/pubmed/21486936) Monolith (https://nanotempertech.com/monolith-mo-control-software/) BLAST package 2.2.6 (Altschul SF et al., 1997, Gapped BLAST and PSI-BLAST: a new generation of protein database search programs. Nucleic Acids Res., 25, 3389-3402) MAFFT v7.123b (Katoh K and Standley DM, 2013, MAFFT multiple sequence alignment software version 7: improvements in performance and usability. Mol. Biol. Evol., 30, 772-780.) HMMER v3.1b1 (Eddy SR, 2009, A new generation of homology search tools based on probabilistic inference. Genome Inform., 23, 205-211. PhyML (Guindon S et al., 2010, New algorithms and mathods to estimate maximum-likelihood phylogenies: assessing the performance of PhyML 3.0. Syst. Biol., 59, 307-321.)

For manuscripts utilizing custom algorithms or software that are central to the research but not yet described in published literature, software must be made available to editors/reviewers upon request. We strongly encourage code deposition in a community repository (e.g. GitHub). See the Nature Research guidelines for submitting code & software for further information.

Data

All manuscripts must include a [data availability statement](#). This statement should provide the following information, where applicable:

- Accession codes, unique identifiers, or web links for publicly available datasets
- A list of figures that have associated raw data
- A description of any restrictions on data availability

The data that support the findings of this study are available from the corresponding author upon request. The ChIP-seq data were deposited at NCBI SRA (accession number PRJNA511435) and GEO (GSE129717).

Field-specific reporting

Please select the best fit for your research. If you are not sure, read the appropriate sections before making your selection.

☒ Life sciences   ☐ Behavioural & social sciences   ☐ Ecological, evolutionary & environmental sciences

For a reference copy of the document with all sections, see [nature.com/authors/policies/ReportingSummary-flat.pdf](#)

Life sciences study design

All studies must disclose on these points even when the disclosure is negative.

Sample size	no sample-size calculation were performed. In bacteria microscopy, it is usual to quantify cells from a whole field, which has given us a minimum sample size of 244 cells.
Data exclusions	no samples were excluded from the analysis.
Replication	All replicates done in identical conditions were similar. SupFig. 18 was performed twice and data in all other figures was performed in triplicate.
Randomization	Samples were not allocated to groups
Blinding	not relevant. no group allocation.

Reporting for specific materials, systems and methods

Materials & experimental systems

n/a	Involved in the study
☐	☒ Unique biological materials
☐	☒ Antibodies
☒	☐ Eukaryotic cell lines
☒	☐ Palaeontology
☒	☐ Animals and other organisms
☒	☐ Human research participants

Methods

n/a	Involved in the study
☐	☒ ChIP-seq
☒	☐ Flow cytometry
☒	☐ MRI-based neuroimaging

Unique biological materials

Obtaining unique materials	all mutant strains constructed and used are readily available from the authors

Antibodies

Antibodies used	Rabbit Anti GFP : TP401 – AMS biotechnology Mouse Anti Flag : Monoclonal ANTI-FLAG M2 F3165 – Sigma Aldrich Goat anti-mouse HRP polyclonal antibody: Biorad, REF 170-6516. Rabbit Anti pneumococcal serotype 2 CPS polyclonal antibody : REF : 16745- Statens serum Institut (Denmark)

Goat anti-anti pneumococcal serotype 2 CPS polyclonal antibody: DyLight TM 549 conjugated AffiniPure Goat anti-Rabbit IgG-Jackson ImmunoResearch Laboratories
Goat Anti Rabbit HRP polyclonal antibody : REF 1706515- Bio-Rad
Rabbit Anti-RocS: Eurogentec
Rabbit anti-Enolase: Fleurie et al, Mol. Microbiol., 2012, 83, 746-758.
Rabbit anti-mKate2: R10367 Thermofisher scientific

Validation

All antibodies were validated in previous studies (Fleurie et al, Mol. Microbiol., 2012, 83, 746-758; Nourikyan et al., PLoS Genet., 2015, 11, e1005518; Zucchini et al., Nat. Microbiol., 2018, 3, 197-209, Nolivos et al., Nat. commun., 2015, 7:10466.) to either detect by western blot, or perform co-immuniprecipitation or cell imaging of GFP, mkate2, FLAG, capsule and the enolase in S. pneumonaie cells.
Anti-rocS antibodies were validated in the present study by western-blot with pure RocS from S. pneumoniae.

ChIP-seq

Data deposition

☒ Confirm that both raw and final processed data have been deposited in a public database such as GEO.

☐ Confirm that you have deposited or provided access to graph files (e.g. BED files) for the called peaks.

Data access links
May remain private before publication.

https://dataview.ncbi.nlm.nih.gov/object/PRJNA511435

Files in database submission

FLAG-RocS whole-cell extract, replicate 1: SRR8363119; FLAG-RocS whole-cell extract, replicate 2: SRR8363120; FLAG-RocS pulldown, replicate 2: SRR8363121

Genome browser session
(e.g. UCSC)

no longer applicable

Methodology

Replicates

Biological duplicate cultures were grown in parallel. Each culture was split into two parts; one for whole-cell extract and one for immunoprecipitation. Due to an insufficient amount of material from one of the immunoprecipitation samples, we collected data on 2 WCE samples and 1 IP sample. With the limited sample number, we were not able to analyze replicate agreement.

Sequencing depth

SRR8363119: 12917510 reads, 11847606 uniquely mapped, 50 nt single-end; coverage: 291
SRR8363120: 13658957 reads, 12529456 uniquely mapped, 50 nt single-end; coverage: 307
SRR8363121: 13470247 reads, 9861206 uniquely mapped, 50 nt single-end; coverage: 242

Antibodies

Anti Flag : Monoclonal ANTI-FLAG M2 F3165 – Sigma Aldrich

Peak calling parameters

Reads were mapped to the S. pneumoniae R6 genome with Bowtie2 with default parameters. The reference genome was artificially extended with 1362 nts (length of dnaA gene) to allow mapping across fasta boundaries. Peak calling was performed with SeqMonk with default parameters, but extending the single-end reads with 200 nts. No significant peaks were detected for any of the individual samples. Therefore, no significant enrichment analysis was performed. In the paper we looked at the highest signals in the coverage plot of the immunoprecipitation sample and subsequently falsified specific binding of RocS to these regions.

Data quality

With our setup, no significant enrichment was detected by SeqMonk, making estimates of false-discovery rate and other useful metrics impossible.

Software

SeqMonk version 1.37.0; bowtie2-align-s version 2.2.6